

Measurement and simulation of residual stresses in transient liquid phase bonded ferritic steels

Nicolás Di Luozzo, Sandra Cabeza, Michel Boudard, Marcelo Fontana

▶ **To cite this version:**

Nicolás Di Luozzo, Sandra Cabeza, Michel Boudard, Marcelo Fontana. Measurement and simulation of residual stresses in transient liquid phase bonded ferritic steels. Journal of Materials Science, 2022, 10.1007/s10853-022-07911-4 . hal-03858380

HAL Id: hal-03858380

https://cnrs.hal.science/hal-03858380

Submitted on 17 Nov 2022

HAL is a multi-disciplinary open access archive for the deposit and dissemination of scientific research documents, whether they are published or not. The documents may come from teaching and research institutions in France or abroad, or from public or private research centers.

L'archive ouverte pluridisciplinaire **HAL**, est destinée au dépôt et à la diffusion de documents scientifiques de niveau recherche, publiés ou non, émanant des établissements d'enseignement et de recherche français ou étrangers, des laboratoires publics ou privés.

Measurement and simulation of residual stresses in transient liquid phase bonded ferritic steels

Nicolás Di Luozzo [a,b,*], Sandra Cabeza [c], Michel Boudard [d], Marcelo Fontana [a,b]

[a] Universidad de Buenos Aires. Facultad de Ingeniería. Laboratorio de Sólidos Amorfos. Paseo Colón 850, Buenos Aires, Argentina.

[b] CONICET – Universidad de Buenos Aires. Instituto de Tecnologías y Ciencias de la Ingeniería "Hilario Fernández Long" (INTECIN). Buenos Aires, Argentina.

[c] Institut Max von Laue – Paul Langevin (ILL), 71 Av. des Martyrs, 38000, Grenoble, France

[d] Université Grenoble Alpes, CNRS, Grenoble INP, LMGP, 38000 Grenoble, France.

[*] Corresponding author
e-mail address: ndiluozzo@fi.uba.ar
ORCID iD: https://orcid.org/0000-0003-3192-3644

Sandra Cabeza
e-mail address: cabeza@ill.fr
ORCID iD: https://orcid.org/0000-0002-6567-1169

Michel Boudard
e-mail address: michel.boudard@grenoble-inp.fr
ORCID iD: https://orcid.org/0000-0001-9596-1346

Marcelo Fontana
e-mail address: mfontan@fi.uba.ar
ORCID iD: https://orcid.org/0000-0002-4861-0997

Abstract

Ferritic steel bars – 25 mm in diameter – were welded by transient liquid phase bonding (TLPB) using Fe-based amorphous metallic foils as filler material. The resulting residual stress (RS) field shows a low peak magnitude – of 147 MPa – as measured by neutron diffraction.

The most distinctive feature of TLPB is the heat input delivered simultaneously at the whole joint that allows much lower cooling rates compared with arc welding (AW). Therefore, the elapsed time between 800 and 500 ºC (*t* 8/5) was particularly long reaching 390 sec. As a result, a low RS peak magnitude (147 MPa) was obtained in the as-welded condition. This value is well below the RS peak magnitude obtained with AW which typically attain the yield strength of the base metal (276 MPa).

The numerical simulation of RS at the welded bars was performed by a thermal and mechanical analysis. It shows that TLPB produced a large austenized region, low cooling rates and a remarkable *t* 8/5. Consequently, the large volume in which the heat input is delivered is the driving force to reduce RS peak magnitudes. From the mechanical analysis, it was found that the simulated RS were in good agreement with the measured RS. Therefore, the proposed numerical simulation model can be used to predict RS in TLPB weldments.

Keywords: ferritic steel; transient liquid phase bonding; residual stress measurement; residual stress numerical simulation.

1. Introduction

Residual stresses (RS) in weldments (the welded assemblies) arise due to unrelieved strains at the joint and the heat affected zone (HAZ). Their sources are due to temperature gradients and/or volume changes induced by phase transformations. RS are added to the in-service stresses and can seriously reduce the performance of weldments.

In arc welding (AW) the heat input $\dot{q}$ is supplied to the surfaces of the workpieces [1–3], generating steep thermal gradients and consequently high cooling rates. As a result, maximum values of RS typically achieve the yield strength σ_y of the base metal – including carbon, low alloy and stainless steels [4–6]. Therefore, welding techniques which produce lower RS and the accurate measurement of the RS field within the weldment are of particular interest.

In transient liquid phase bonding (TLPB) [7] the whole joint is heated to the process temperature (T_P) below the melting point of the base metal and above the melting point of the filler material. The temperature is then held constant at T_P during a preset time (t_h) and finally the whole joint is cooled down to ambient temperature in still air or using an inert or reducing atmosphere. This thermal cycle at the joint allows the generation of low cooling rates. For ferritic steels, the elapsed time between 800 and 500 ºC (t 8/5) – range of temperature in which the austenite transformation takes place, is particularly long [8]. As a result, TLPB has a great potential to develop low RS.

Of all non-destructive techniques to measure RS, diffraction methods are widely accepted as the most reliable ones. In particular, neutron diffraction (ND) is the only one capable of measuring RS inside the weldment, with a millimetric spatial resolution and a cube-shaped gauge volumes (≈ 10 mm^3 in size) [9] [1]. This clearly improves upon the elongated diamond shape gauge volumes obtained in high energy synchrotron X-ray diffraction experiments [10].

For the first time, we have investigated RS in TLPB ferritic steel weldments using Fe-based amorphous metallic foils as filler material. RS measurements were performed by ND, while RS modelling was carried out with a thermal and mechanical analysis. The main outcomes of the present work are:

[1] It is worth noting that the usefulness of measuring RS by ND depends on the specimen dimensions. For small specimens, the gauge volume for ND can be very large (e.g.: It may capture both the fusion zone and the heat affected zone).

- The low cooling rates achieved by TLPB reduces considerably the magnitude of RS measured at the joint and the HAZ in the as-welded condition.
- The numerical simulation of the RS in TLPB ferritic steel weldments are in good agreement with the measured RS. Therefore, the proposed simulation model can be used to predict RS in TLPB weldments.

2. Materials and methods

2.1. TLPB procedure

The base metal consisted in hot-wrought carbon steel bars ASTM A29 1011 [11] 150 mm long and 25 mm in diameter. This base metal had a σ_y = 276 MPa as measured by tensile tests according to ASTM E8 [12]. Regarding the filler material positioned between the bars to be welded, a Metglas® SA1 amorphous metallic foil of the Fe-Si-B system with a thickness of 25 μm was used. It is worth noting that the ductility of this amorphous metallic foil enabled its handling even in this range of thicknesses. The chemical compositions of the base metal and the filler material are shown in Table 1.

Table 1

Chemical compositions (in wt.%) of the base metal and the filler material.

	C	Mn	Si	P	Ni	Cr	Mo	Cu	Sn	B	Fe
Grade 1011	0.11	0.78	0.17	0.09	0.06	0.06	0.010	0.14	0.01		Bal.
SA1			5							3	Bal.

The joint and its adjacent base metal were subjected to the following thermal cycle:

- heated to T_P = 1300 ºC,
- held at T_P during t_h = 7 min,
- cooled down to ambient temperature in still air.

The necessary $\dot{q}$ during the heating and holding stages was supplied by an induction furnace (its power was cut off during the cooling stage). In addition, an uniaxial pressure of 4 MPa was applied during the thermal cycle and part of the heated zone was protected by a reducing atmosphere (Ar + 10% H_2) contained by a concentric PIREX® tube – hereafter the protected surface – to minimize scale formation. The temperature at

the joint was controlled by means of a type K thermocouple. A cutaway drawing of the TLPB layout is provided in Fig. 1.

Field-emission gun-scanning electron microscopy (Zeiss Ultra 55) was used to determine the microstructures of the base metal, the HAZ and the joint. Sample preparation consisted in grinding, polishing, and final etching with 2% Nital solution.

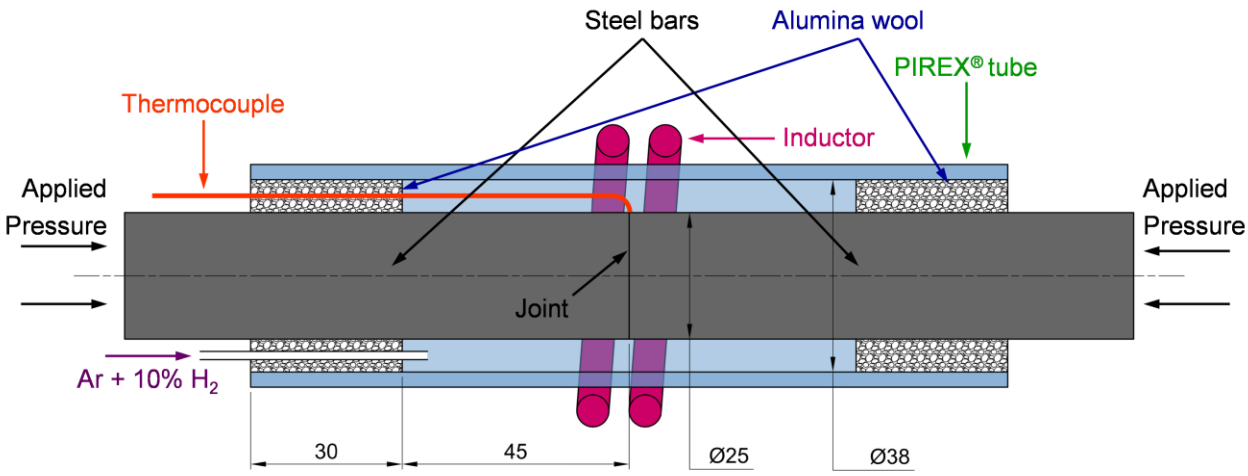


Fig. 1 Cutaway drawing of the TLPB layout. The relative position of the joint, the steel bars, the inductor of the induction furnace, the thermocouple and the protecting PIREX® tube are indicated. Alumina wool was used as seal between the bars and the protecting tube while the reducing atmosphere was injected through the wool. The applied pressure is indicated and characteristic dimensions in mm are included

2.2. Neutron Residual Stress characterization

ND scanning was carried out at the strain diffractometer for engineering applications SALSA at the Institut Max von Laue – Paul Langevin (ILL) in Grenoble, France [13].

The measurements at this monochromatic instrument were performed under a neutron beam wavelength of 1.71713 Å. The α-Fe 211 Bragg reflection was analysed since it is the most representative of the macroscopic behaviour for a BCC structure [14].

The gauge volume was defined by radial collimators to 2x2x2 mm^3. Data reduction was performed with LAMP in-house software [15], considering a symmetrical Gaussian profile and an adjusted background function, allowing to obtained the Bragg angle at each location of the sample.

The normal strain ε_{ii} of the strain tensor $\boldsymbol{\varepsilon}$ for a direction i and a plane (hkl) is defined as follows:

$$\varepsilon_{ii\,hkl} = \frac{d_{ii\,hkl} - d_{0\,hkl}}{d_{0\,hkl}} \quad (1)$$

where d_{ii} and d_0 are respectively the actual and stress-free lattice spacing, respectively.
In our case, ε_{ii} was measured at each point in the radial direction (r), the circumferential direction (θ) and the axial direction (z).
Finally, the normal stresses σ_{ii} of the stress tensor $\boldsymbol{\sigma}$ at each point can be calculated considering the strain in each direction and Hooke's law as:

$$\sigma_{ii\,hkl} = \frac{Y_{hkl}}{(1+\nu_{hkl})(1-2\nu_{hkl})}\left[(1-\nu_{hkl})\varepsilon^{e}_{ii\;hkl} + \nu_{hkl}\sum \varepsilon^{e}_{jj\;hkl}\right] \quad (2)$$

where:

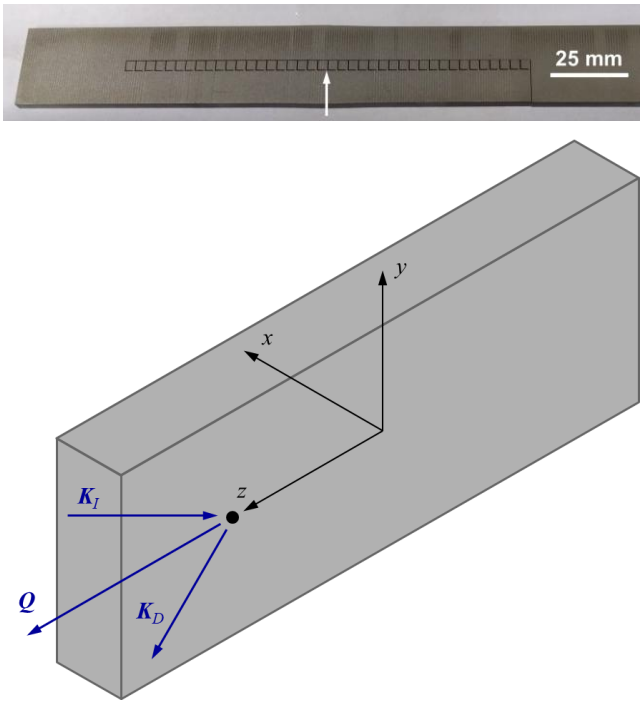
- Y_{hkl} is the Young's modulus for the plane (hkl)
- ν_{hkl} is the Poisson's ratio for the plane (hkl)
- $i = r, \theta, z$
- $j = r, \theta, z; j \neq i$
- hkl = 211

The diffraction elastic constants based on a Kröner model [16] for α-Fe 211 were Y_{211} = 217 GPa and ν_{211} = 0.277.
It is worth noting that to avoid changes between the centre of gravity of the gauge volume and the scattering volume, ND was carried out up to a radius that assured that the gauge volume was fully immersed into the base metal (i.e. avoiding pseudo-strain effect) [17].
For further information on data analysis please check reference [14].

2.3. Measurement of the stress-free lattice spacing

A reference sample for d_0 measurement was prepared as a comb and measured as a function of the distance from the joint. This sample was cut – from another weldment performed identically to those where RS were measured – by wire-cut electrical discharge machining (WEDM). In this sample, cubes were also cut by WEDM, with their centres along the axis of the bar. The volume of each of cube was 3x3x3 mm^3, to allow the whole neutron gauge to be immersed while characterizing the macroscopically relaxed condition (Fig. 2, top panel). This condition was attained with the described cutting procedure. WEDM is practically a distortion-free cutting process, avoiding the addition of further RS to the cubes due to the cutting procedure [18].

At each cube, d_0 was measured in z (Fig. 2, middle panel) and x (Fig. 2, bottom panel) directions and an average value was determined to use for strain/stress calculations.



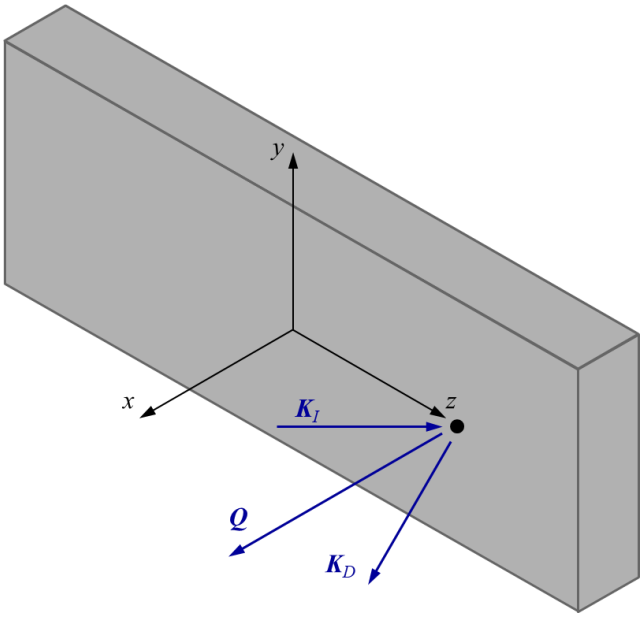


Fig. 2 Reference sample. Top panel: actual reference sample where the average d_0 vs. distance from the joint (z) was measured (the position of the joint is indicated by an arrow mark). Layout to measure d_0 in z (middle panel) and x directions (bottom panel). The black point is indicating the centre of a cube, with the corresponding incident beam wavevector ($\boldsymbol{K}_I$), diffracted beam wavevector ($\boldsymbol{K}_D$) and scattering vector ($\boldsymbol{Q}$)

The measured d_0 in the z and x directions, and the average d_0 – at each of the centres of the cubes of the reference sample – as a function of the distance from the joint (z) (see Fig. 2, top panel) are shown in Fig. 3. In this way, chemical composition gradients that may change d_0 along z axis are directly considered.

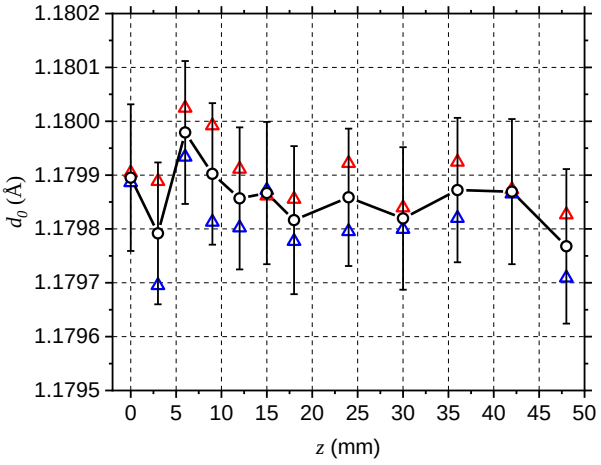


Fig. 3 d_0 vs distance from the joint (z) for the reference sample. Measurements of d_0 in the z direction (red triangle marks), x direction (blue triangle marks) and their average

(open circle marks) are shown. In addition, and for ease of expression and comprehension, only the error bars for the average d_0 are indicated

2.4 Weldment scanning

Strain scanning of the weldment was performed in r, θ, and z directions – with the corresponding $\boldsymbol{K}_I$, $\boldsymbol{K}_D$, and $\boldsymbol{Q}$ – as it is shown in Fig. 4. The θ layout was obtained by rotating the weldment 90º in z axis with respect to the r layout, and the z layout by subsequently tilting the weldment 90º with respect to the previous one.

It is worth noting that based on the axisymmetric geometry of the bars to be welded and of the heat input, the following symmetry operations were assumed:

- $z = 0$
- z axis

Therefore, the strain scanning for each direction was performed in the second quarter of the yz plane, with -11 mm $< y < 0$ and $0 < z < 48$ mm.

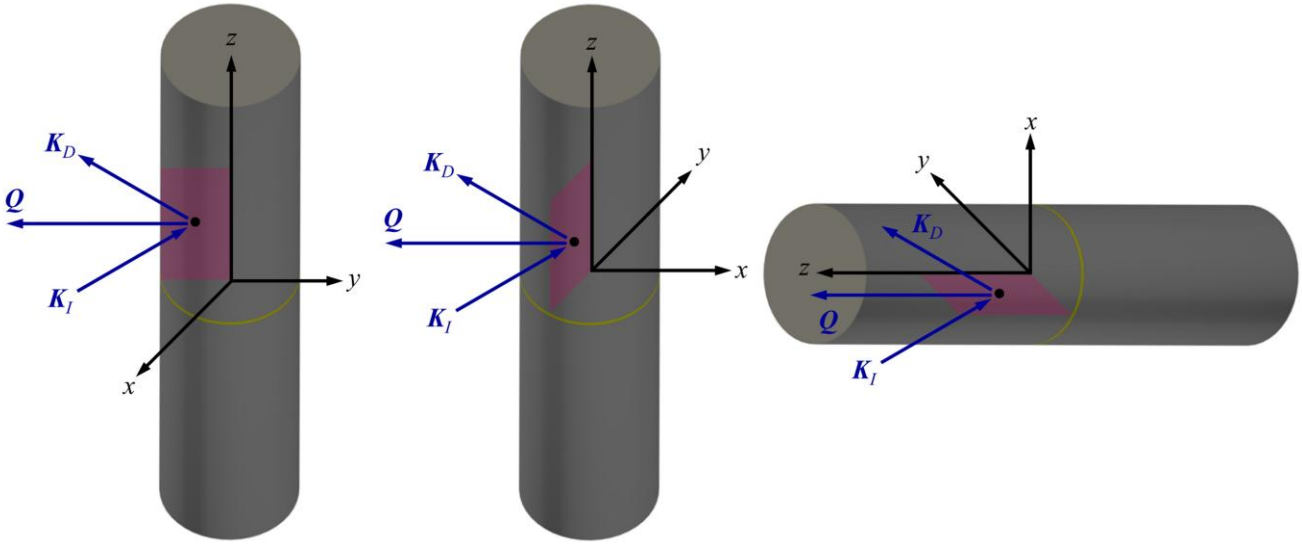


Fig. 4 Scheme of the strain scanning layout and scanned areas for each measured direction: r (left), θ (centre) and z (right). Light red areas show the scanned area in each layout (out of scale). Also, the joint position is indicated (yellow line). In each scanned area a point of measurement (black dot) is shown with the corresponding $\boldsymbol{K}_I$, $\boldsymbol{K}_D$ and $\boldsymbol{Q}$. The xyz coordinate system fixed to the weldment is indicated

3. Analysis of residual stresses by numerical simulation

3.1. Generation mechanism of residual stresses in welding

During welding, a large amount of $\dot{q}$ is supplied at the joint. The temperature distribution is not uniform and changes with time, which causes different magnitude of thermal strains in the joint and the HAZ. In addition, this uneven temperature distribution can cause inhomogeneous volume changes induced by solid-state phase transformations.

To adjust the different strains in the joint and the HAZ, elastic strains and/or plastic strains are produced and consequently result in stresses.

The most important assumption to simulate this problem is that $\boldsymbol{\varepsilon}$ can be decomposed into the sum of:

$$\boldsymbol{\varepsilon} = \boldsymbol{\varepsilon}^{e} + \boldsymbol{\varepsilon}^{p} + \boldsymbol{\varepsilon}^{th} + \boldsymbol{\varepsilon}^{tr} \quad (3)$$

where $\boldsymbol{\varepsilon}^{e}$, $\boldsymbol{\varepsilon}^{p}$, $\boldsymbol{\varepsilon}^{th}$ and $\boldsymbol{\varepsilon}^{tr}$ are the elastic, plastic, thermal and phase transformation strain tensors [19].

However, it is a highly nonlinear problem, and it is solved incrementally by numerical simulation. In the incremental solution process, the time is divided into small increments – from now on time steps Δt. Thus, the increment of the strain tensor $\Delta\boldsymbol{\varepsilon}$ can be expressed as [20]:

$$\Delta\boldsymbol{\varepsilon} = \Delta\boldsymbol{\varepsilon}^{e} + \Delta\boldsymbol{\varepsilon}^{p} + \Delta\boldsymbol{\varepsilon}^{th} + \Delta\boldsymbol{\varepsilon}^{tr} \quad (4)$$

If $\boldsymbol{\varepsilon}^{tr}$ can be included as a part of $\boldsymbol{\varepsilon}^{th}$, an effective thermal strain tensor $\boldsymbol{\varepsilon}^{th\,ef}$ can be obtained. This simplification has indeed been used in literature [21, 22] and therefore, for a given Δt, $\Delta\boldsymbol{\varepsilon}^{th\,ef}$ can be written as:

$$\Delta\boldsymbol{\varepsilon}^{th\,ef} = \Delta\boldsymbol{\varepsilon}^{th} + \Delta\boldsymbol{\varepsilon}^{tr} = \alpha\Delta T\boldsymbol{\delta} + \Delta\boldsymbol{\varepsilon}^{tr}$$

$$\Delta\boldsymbol{\varepsilon}^{th\,ef} = \alpha_{ef}\Delta T\boldsymbol{\delta}$$

where α and α_{ef} are the linear and the effective thermal expansion coefficient, ΔT is the temperature increment and $\boldsymbol{\delta}$ the Kronecker tensor, respectively. Thus, equation (4) can be rearranged as follows:

$$\Delta\boldsymbol{\varepsilon} = \Delta\boldsymbol{\varepsilon}^{e} + \Delta\boldsymbol{\varepsilon}^{p} + \Delta\boldsymbol{\varepsilon}^{th\,ef}$$

$$\Delta\boldsymbol{\varepsilon} = \Delta\boldsymbol{\varepsilon}^{e} + \Delta\boldsymbol{\varepsilon}^{p} + \alpha_{ef}\Delta T\boldsymbol{\delta}$$

As a result, we have that:

- The RS generation mechanism was assumed as the result of the uneven thermal strain field.

- To calculate RS field in the weldment the simulation procedure must compute the elastic, plastic and thermal strain fields.

3.2. Formulation of the thermal analysis

The temperature field in the steel bars satisfied the Fourier's conduction law in the axisymmetric case:

$$\lambda\left(\frac{\partial^2 T}{\partial r^2}+\frac{1}{r}\frac{\partial T}{\partial r}+\frac{\partial^2 T}{\partial z^2}\right)+\dot{q}=\rho C_P\frac{\partial T}{\partial t}$$

where λ, ρ and C_P are the thermal conductivity, density and specific heat, respectively. In our particular case, $\dot{q}$ was supplied by an induction furnace and was calculated as follows [23]:

$$\dot{q}=\kappa|\boldsymbol{E}|^2$$

where κ is the electrical conductivity and $\boldsymbol{E}$ is the electric field. For the formulation to determine $\boldsymbol{E}$, see references [24, 25].

The following radiation and convection boundary conditions were used (Fig. 5):

- On the protected and bare surfaces of the weldment:

  $$\lambda\nabla T\cdot\boldsymbol{n}+h_{Protected}(T-T_{amb})+e_{Protected}\,\sigma_{sb}(T^4-T_{amb}{}^4)=0$$
  $$\lambda\nabla T\cdot\boldsymbol{n}+h_{Bare}(T-T_{amb})+e_{Bare}\,\sigma_{sb}(T^4-T_{amb}{}^4)=0$$

  where $\boldsymbol{n}$ is the surface unit normal, h is the convection coefficient, e is the surface emissivity, T_{amb} is the ambient temperature and σ_{sb} is the Stefan-Boltzmann constant (5.67×10^{-8} W/m^2 K^4).
- An insulation condition was applied at the surface in contact with the alumina wool:

  $$\lambda\nabla T\cdot\boldsymbol{n}=0$$

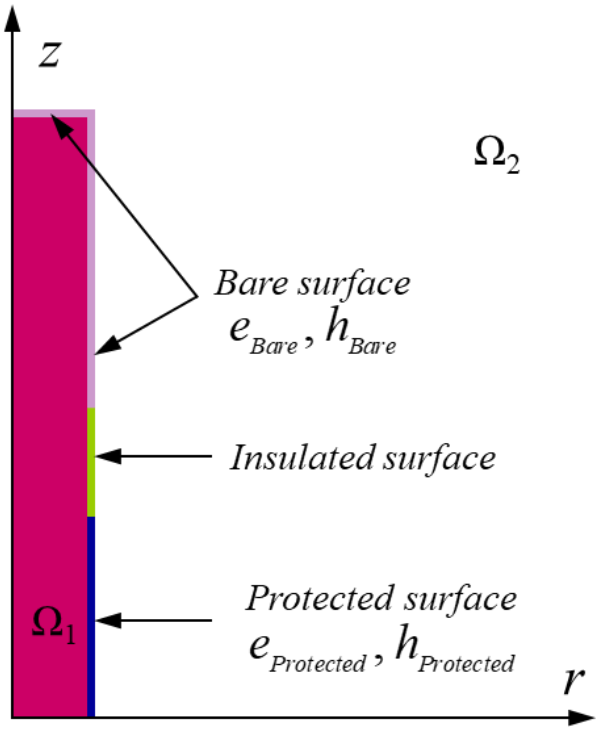


Fig. 5 Boundary conditions for the thermal analysis. The bare (light violet), insulated (light green) and protected (blue) surfaces are indicated. In addition, the conducting region – the steel bar (Ω_1) – and the nonmagnetic region – the rest of the domain (Ω_2) – are denoted

The simulations were performed with ELMER FEM software package [26] using 2-D axisymmetric 3-node linear triangular elements. The weldment was meshed using 41505 nodes and 20256 elements.

The physical properties used in the thermal analysis were:

- ρ = 7850 kg/m^3 [27]
- λ (W/mº C) [27]

$$\begin{cases} 54 - 3.33\times10^{-2}T & 20\,^{\circ}\mathrm{C} < T < 800\,^{\circ}\mathrm{C} \\ 27.3 & T > 800\,^{\circ}\mathrm{C} \end{cases}$$

- C_P (J/kg K) [27]

$$\begin{cases} 425 + 7.73\times10^{-1}T - 1.69\times10^{-3}T^2 + 2.22\times10^{-6}T^3 & 20\ ^{o}\text{C} < T < 600\ ^{o}\text{C} \\ 666 + \dfrac{13002}{738 - T} & 600\ ^{o}\text{C} < T < 735\ ^{o}\text{C} \\ 545 + \dfrac{17820}{T - 731} & 735\ ^{o}\text{C} < T < 900\ ^{o}\text{C} \\ 650 & 900\ ^{o}\text{C} < T < 1300^{o}\text{C} \end{cases}$$

- A mean value for $e_{Bare} = e_{Protected} = 0.22$ was selected [28].
- At the bare surfaces of the bars, h_{Bare} was calculated using the correlation of Churchill and Chu [29], obtaining $h_{Bare} = 12.5$ W/m^2 ºC.
- At the protected surfaces of the bars, $h_{Protected}$ was calculated using the correlation of Raithby and Hollands [30], obtaining $h_{Protected} = 35$ W/m^2 ºC.

3.3. Formulation of the mechanical analysis

The equations governing the equilibrium of a body in the axisymmetric case are:

$$\begin{aligned} &\frac{\partial \sigma_{rr}}{\partial r} + \frac{\partial \sigma_{rz}}{\partial z} + \frac{\sigma_{rr} - \sigma_{\theta\theta}}{r} = 0 \\ &\frac{\partial \sigma_{zz}}{\partial z} + \frac{\partial \sigma_{rz}}{\partial r} + \frac{\sigma_{rz}}{r} = 0 \end{aligned} \qquad (5)$$

neglecting body forces (e.g.: gravity).

Taking into account equation (3) and the Hooke's law for an isotropic elastic material σ_{ij} can be written as follows [19]:

$$\begin{aligned} &\sigma_{ij} = C_{ijrs}\ \varepsilon_{rs}{}^{e} = C_{ijrs}\left(\varepsilon_{rs} - \varepsilon_{rs}{}^{p} - \varepsilon_{rs}{}^{th\,ef}\right) \\ &i, j, r, s = r, \theta, z \end{aligned} \qquad (6)$$

$$C_{ijrs} = \Lambda\delta_{ij}\delta_{rs} + G(\delta_{ir}\delta_{js} + \delta_{is}\delta_{jr})$$

$$\Lambda = \frac{Y\,\nu}{(1+\nu)(1-2\nu)} \qquad G = \frac{Y}{2(1+\nu)}$$

where C_{ijrs} is the elasticity tensor, Λ is the Lamé's constant and G is the shear modulus.

However, to solve the equations (5) and (6), a criterium to calculate $\boldsymbol{\varepsilon}^{p}$ must be determined if elastoplasticity is taking place. To that end, the von Mises yield criterium was used, comprising an isotropic strain hardening rule [31].

The following displacement boundary condition were prescribed (Fig. 6):

- $u_r = 0$ at $r = 0$
- $u_z = 0$ at $z = 0$
- $u_r = u_z = 0$ at $r = z = 0$

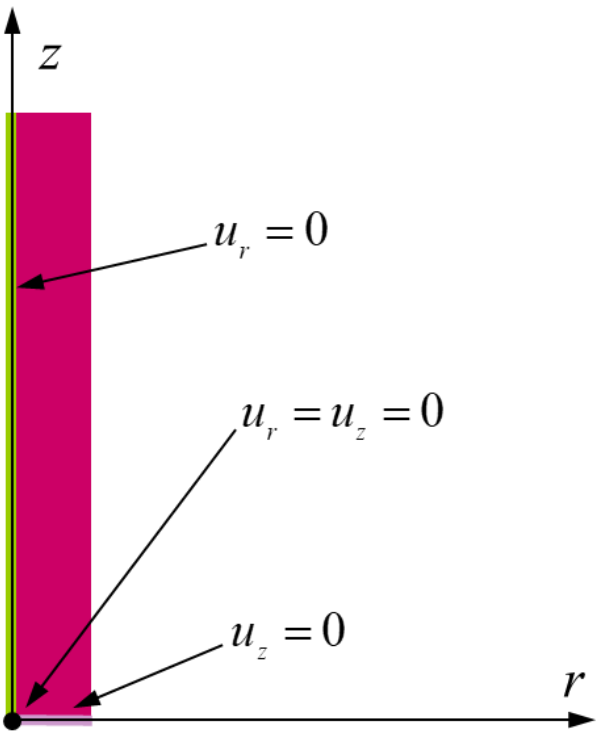


Fig. 6 Displacement boundary conditions at the weldment. Constraints were applied at the axis of symmetry (u_r = 0, light green line), at z = 0 (u_z = 0, light violet line) and at the origin (fixed point, black circle mark)

The simulations were performed with Code_Aster software package [32] using 2–D axisymmetric quadrilateral bilinear elements. The weldment was meshed using 51961 nodes and 51300 elements.

The following physical properties were used for the mechanical analysis:

- Y, the elastic proportional limit (σ_{prop}) and σ_y were taken from the Eurocode 3: Design of steel structures – Part 1-2: General rules – Structural fire design (EC3) [27]. Fig. 7 shows the reduction factor k for Y, σ_{prop} and σ_y at elevated temperature, where:

$$k_Y(T) = \frac{Y(T)}{Y(20\,^{o}C)}; \quad k_{\sigma_{prop}}(T) = \frac{\sigma_{prop}(T)}{\sigma_{prop}(20\,^{o}C)}; \quad k_{\sigma_y}(T) = \frac{\sigma_y(T)}{\sigma_y(20\,^{o}C)}$$

- α_{ef} is defined as follows:

$$\alpha_{ef} = \frac{1}{L_0}\frac{\Delta L}{\Delta T}$$

where L_0 is the initial length of the sample. Liu *et al* [33] reported α_{ef} measurements for carbon steels at cooling rates from 5 to 20 ºC/min – the latter being selected both for the heating and cooling stage (Fig. 8).

- v: Stang *et al* [34] reported a mean value of 0.27 in the elastic range for low carbon steel at ambient temperature.

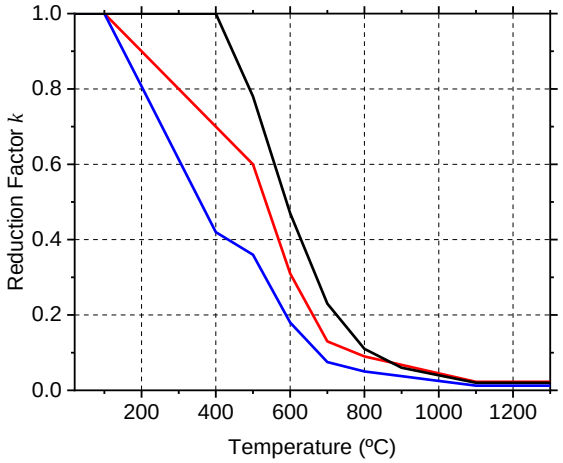


Fig. 7 Reduction factor k from ambient to elevated temperature for Y (red line), σ_{prop} (blue line) and σ_y (black line)

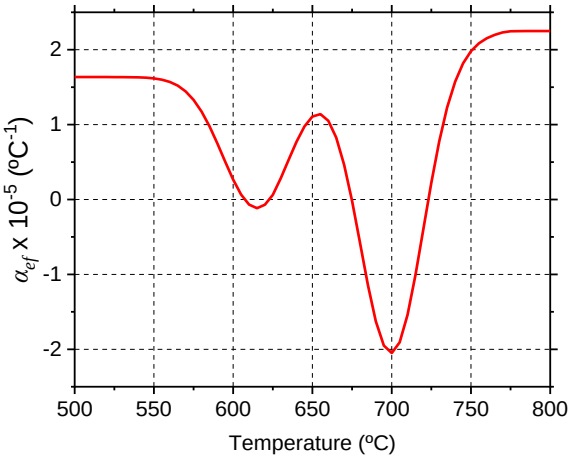


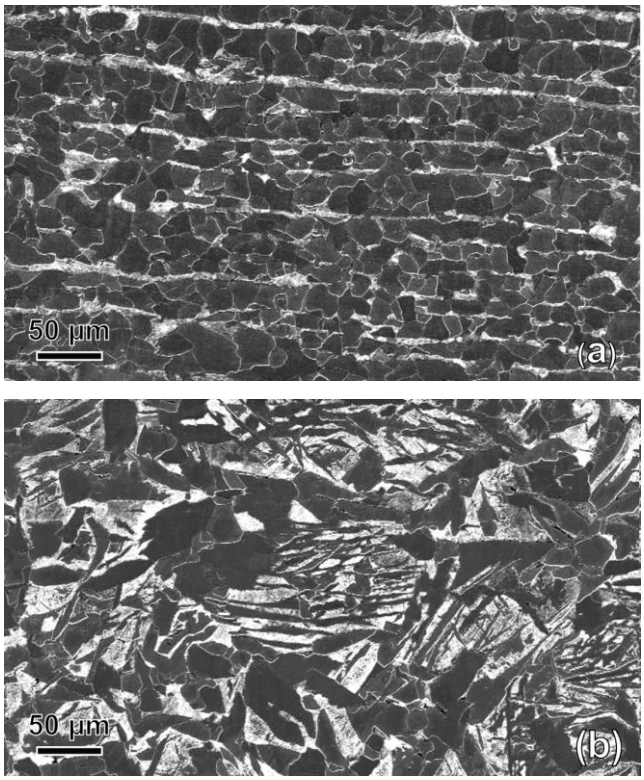
Fig. 8 α_{ef} vs temperature during cooling. The dips at 700 and 615 ºC are indicating the austenite/ferrite and austenite/pearlite phase transformations, respectively [33]

4. Results

4.1. Microstructure at the joint and the heat affected zone

Both at the base metal (Fig. 9 (a)) and at the HAZ (Fig. 9 (b)) a ferritic/pearlitic microstructure was observed. However, the grain growth at the HAZ due to the thermal cycle was clearly visible. Regarding the joint, it was composed of a column of ferrite grains perpendicular to *z* direction (≈ 50-90 μm in width), with ferrite and pearlite adjacent to it (Fig. 9 (c)).

Therefore, the joint and the HAZ had the same microconstituents as the base metal, and α-Fe 211 Bragg reflection in ND scanning could be measured both at ferrite grains and ferrite lamellae of pearlite.



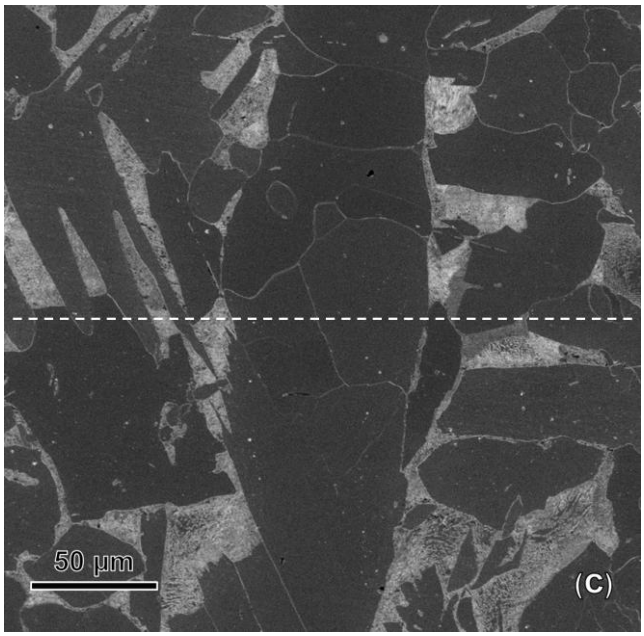


Fig. 9 Microstructure of the weldment at: the base metal (a), the HAZ (b) and the joint (c). The column of ferrite grains at the joint clearly contrasts with the nearby ferritic/pearlitic microstructure. The *z* direction of the weldment (dashed line) is indicated

4.2. Measured and simulated temperature at the joint

The temperature was measured at the joint during TLPB (Fig. 10, red circular marks) to determine its agreement with the simulated thermal analysis. The simulated temperature at the joint (Fig. 10, blue line) has a good matching with the measured data.

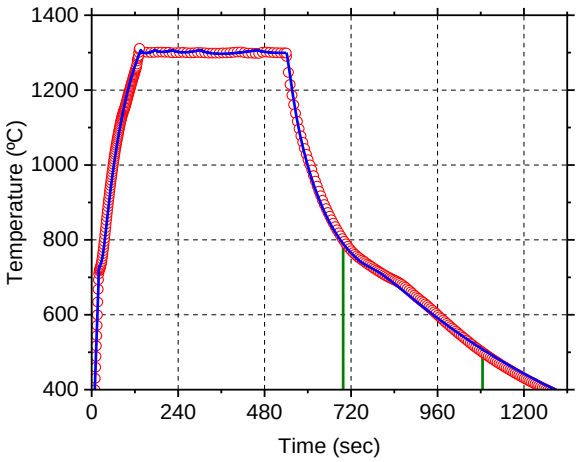


Fig. 10 Temperature evolution at the joint during TLPB. For the measured data (red circular marks) the elapsed time *t* 8/5 = 390 sec is indicated (green solid lines). In

addition, the temperature at the joint obtained from the thermal-structural analysis (see Section 3.2) is shown (blue line)

4.3. Residual Stress Characterization

With the ε_{rr}, ε_{zz} and $\varepsilon_{\theta\theta}$ measured by means of ND strain scanning of the weldment and equations (1) and (2) RS maps for each direction were obtained and are showed in Fig. 11. For each of them, two distinct regions (deep blue colour in Fig. 11) have RS peak magnitudes associated with compressive stress states:

- At the joint: $0 < z < 10$ mm
- Far from the joint: 40 mm $< z <$ 48 mm

The RS peak magnitudes associated with compressive stress states attained 140 MPa (50.7% σ_y), 147 MPa (53.3% σ_y) and 145 MPa (52.5% σ_y) for σ_{rr}, σ_{zz} and $\sigma_{\theta\theta}$ respectively. This compressive stress state is observed at least in the core of the weldment – the region that extents up to y = 8 mm, and in the whole scanned area for σ_{rr} and $\sigma_{\theta\theta}$.

In addition, for σ_{zz} tensile RS reach up to y = 10 mm, with a peak value of 47 MPa.

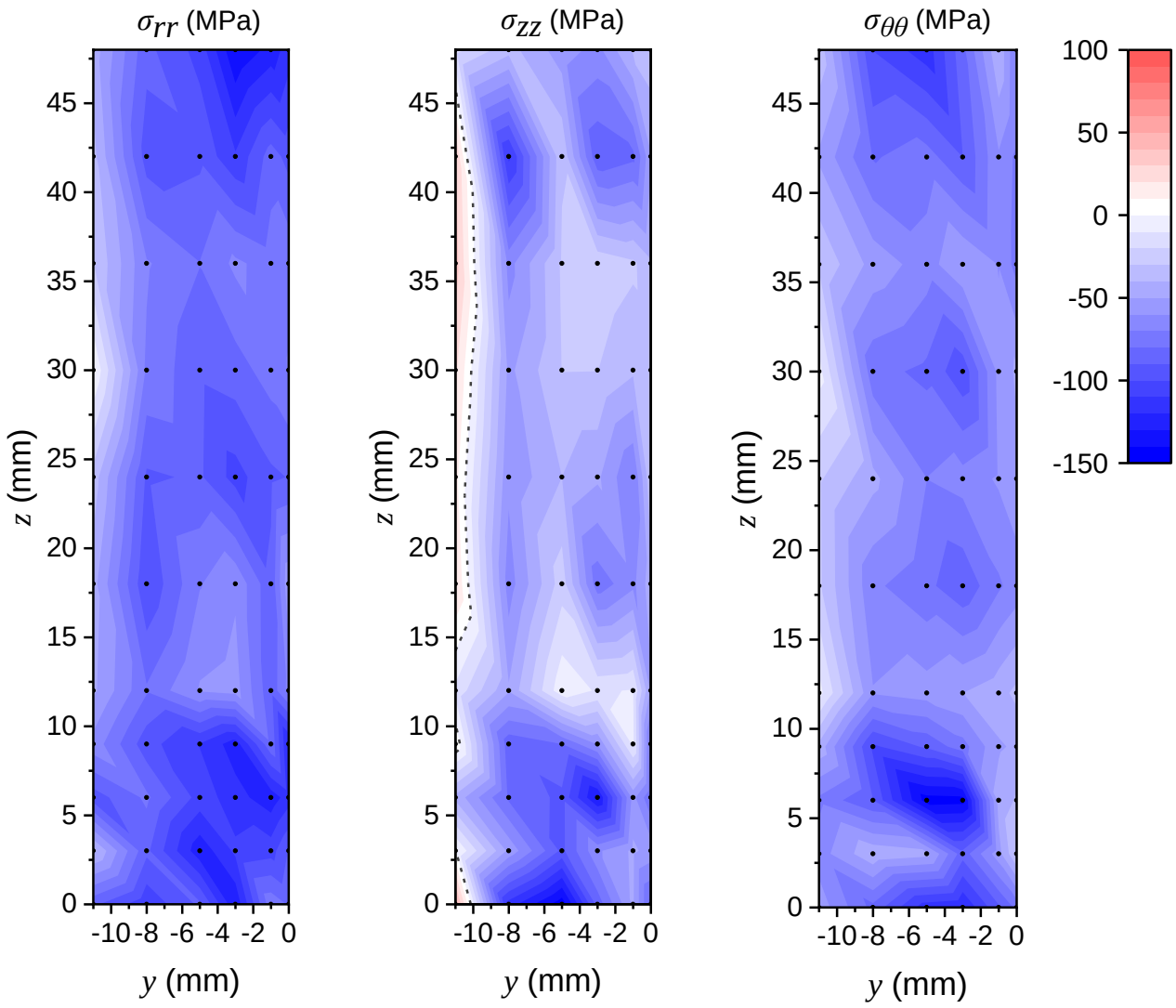


Fig. 11 Measured RS scanning at the weldment for σ_{rr}, σ_{zz}, and $\sigma_{\theta\theta}$. The measured points are indicated with black dots. Dashed line: $\sigma_{ii} = 0$ for $i = r, \theta, z$

4.4. Simulated residual stresses at the weldment

Fig. 12 shows the simulated RS obtained from the thermal and structural analysis. As for the experimental values, the core of the weldment is under a compressive stress state and RS peak magnitudes are also observed at the joint and far from the joint.

In addition, it can be observed that:

- For σ_{zz}, the compressive RS peak far from the joint is observed closer from the joint compared with σ_{rr} and $\sigma_{\theta\theta}$.

- For σ_{zz} and $\sigma_{\theta\theta}$, tensile RS reach the core of the weldment. In particular, for σ_{zz} a tensile RS peak magnitude of 99 MPa was obtained. Therefore, a slight overestimation of the tensile RS is observed outside the core of the weldment.

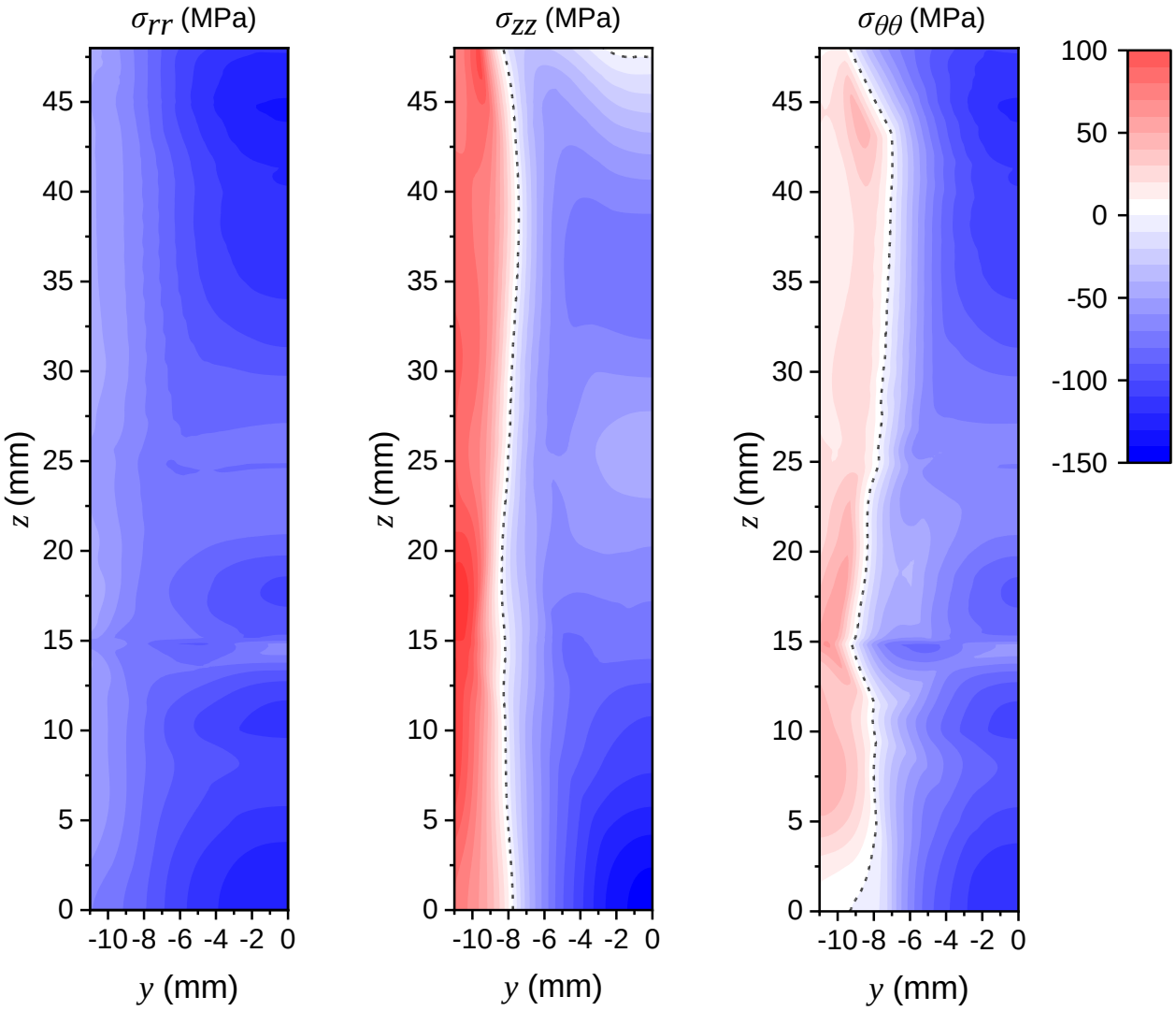


Fig. 12 Simulated RS at the weldment for σ_{rr}, σ_{zz}, and $\sigma_{\theta\theta}$. Dashed line: $\sigma_{ii} = 0$ for $i = r, \theta, z$

5. Discussion

5.1. Agreement between the simulated and the measured residual stresses

The simulated and measured σ_{rr}, σ_{zz} and $\sigma_{\theta\theta}$ were compared along the z direction as follows:

- $y = 0$ mm, at the symmetry axis of the welded bars (Fig. 13)

- y = – 1 mm (Fig. 14)
- y = – 3 mm (Fig. 15)
- y = – 5 mm (Fig. 16)
- y = – 8 mm (Fig. 17)
- y = – 11 mm, nearby the outer surface (Fig. 18)

For a measured RS at a given point, it was considered that a good agreement was reached when the simulated data was within two times the average uncertainty value of the measurement (the average uncertainty value was 41 MPa).

The data set contains 18 comparisons along the z direction of the simulation against the experimental values. The simulated values were:

- Estimating very well the experimental data for a considerable part of the data set (10 of 18 comparisons)
- Underestimating the experimental data for σ_{zz} and $\sigma_{\theta\theta}$ at y = 0 mm (Fig. 13) and y = – 1 mm (Fig. 14)
- Overestimating the experimental data for σ_{zz} and $\sigma_{\theta\theta}$ at y = – 8 mm (Fig. 17) and y = – 11 mm (Fig. 18)

Therefore, the simulated values were properly reproducing most part of the data ranging from y = 0 mm to y = – 11 mm. Some systematic overestimation occurred for absolute values of the RS near y = 0 mm and y = – 11 mm, but it is very difficult to assess its origin. For example, they could be related to parameters used in the thermal and mechanical analysis – the physical properties were assumed as constants or temperature dependent selected from the available literature, and/or to the experimental setup – the symmetry conditions could not be strictly met due to slight misalignments.

Nevertheless, in 92.4% on the measured positions the simulated values were within two times the average uncertainty value of the measurement. Therefore, a good agreement was obtained between the simulated and measured RS.

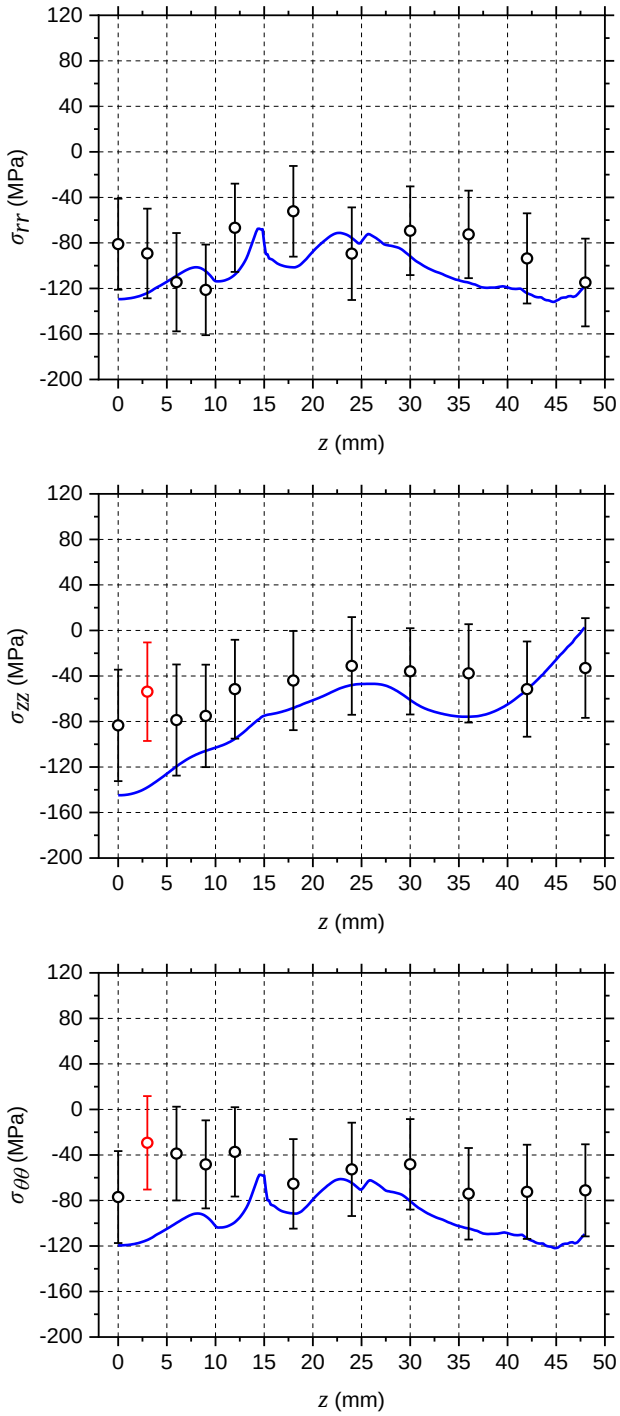


Fig. 13 Measured (circle marks) vs simulated RS (solid line) as a function of the distance from the joint (z) at y = 0 mm for σ_{rr}, σ_{zz} and $\sigma_{\theta\theta}$. The error bars of data points are also shown. Red symbols: positions in which the measured and simulated RS are not in good agreement

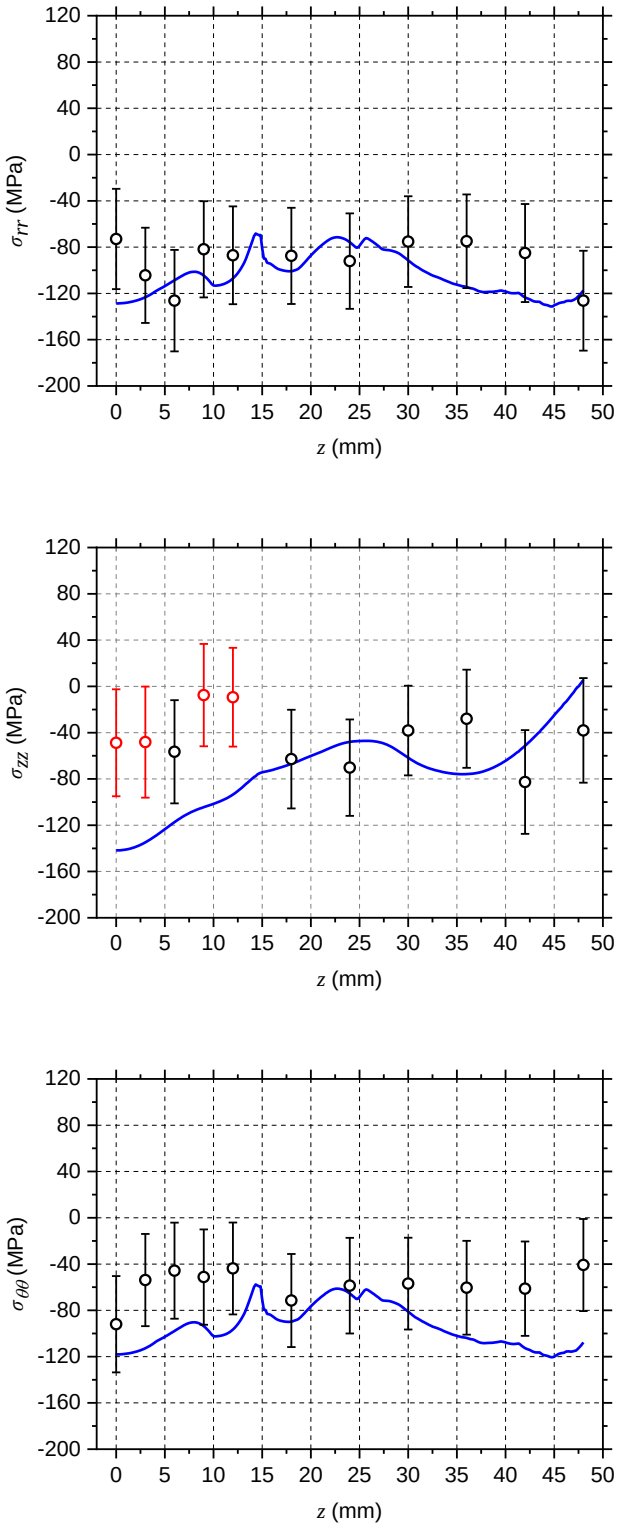


Fig. 14 Measured (circle marks) vs simulated RS (solid line) as a function of the distance from the joint (z) at y = – 1 mm for σ_{rr}, σ_{zz} and $\sigma_{\theta\theta}$. The error bars of data points are also shown. Red symbols: positions in which the measured and simulated RS are not in good agreement

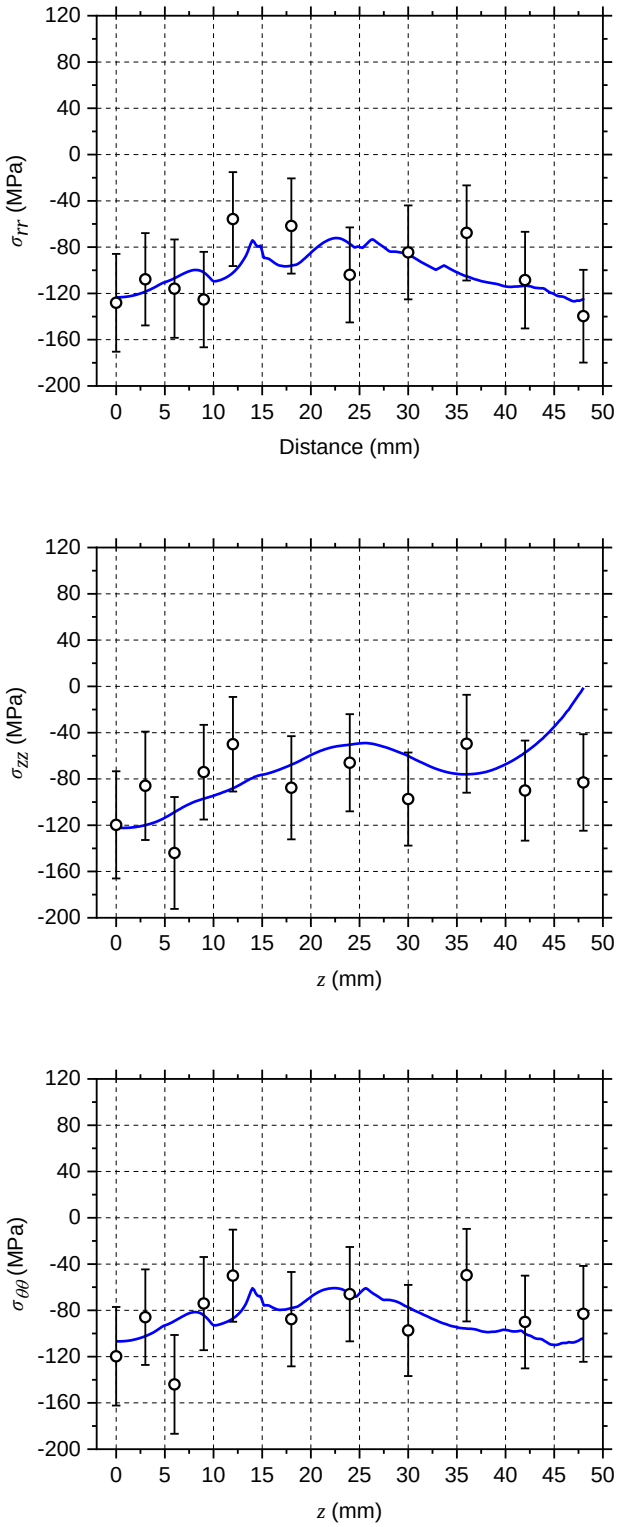


Fig. 15 Measured (circle marks) vs simulated RS (solid line) as a function of the distance from the joint (z) at y = – 3 mm for σ_{rr}, σ_{zz} and $\sigma_{\theta\theta}$. The error bars of data points are also shown. At all positions the measured and simulated RS are in good agreement

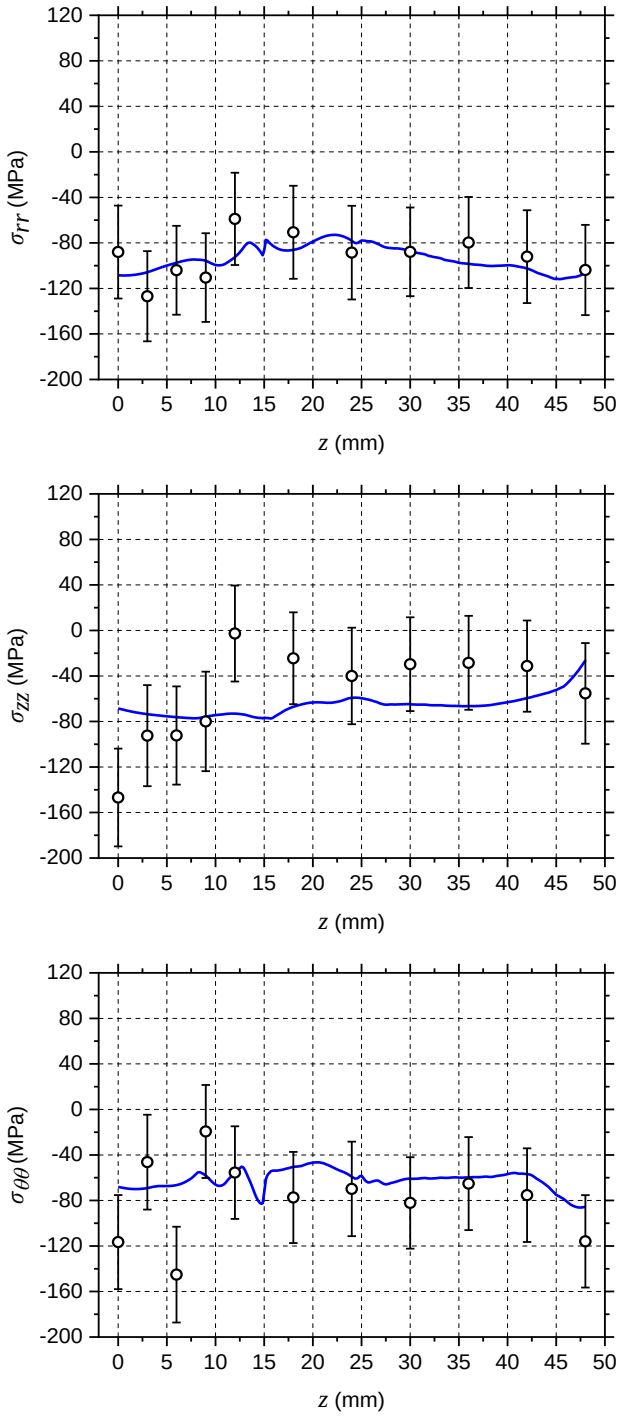


Fig. 16 Measured (circle marks) vs simulated RS (solid line) as a function of the distance from the joint (z) at y = – 5 mm for σ_{rr}, σ_{zz} and $\sigma_{\theta\theta}$. The error bars of data points are also shown. At all positions the measured and simulated RS are in good agreement

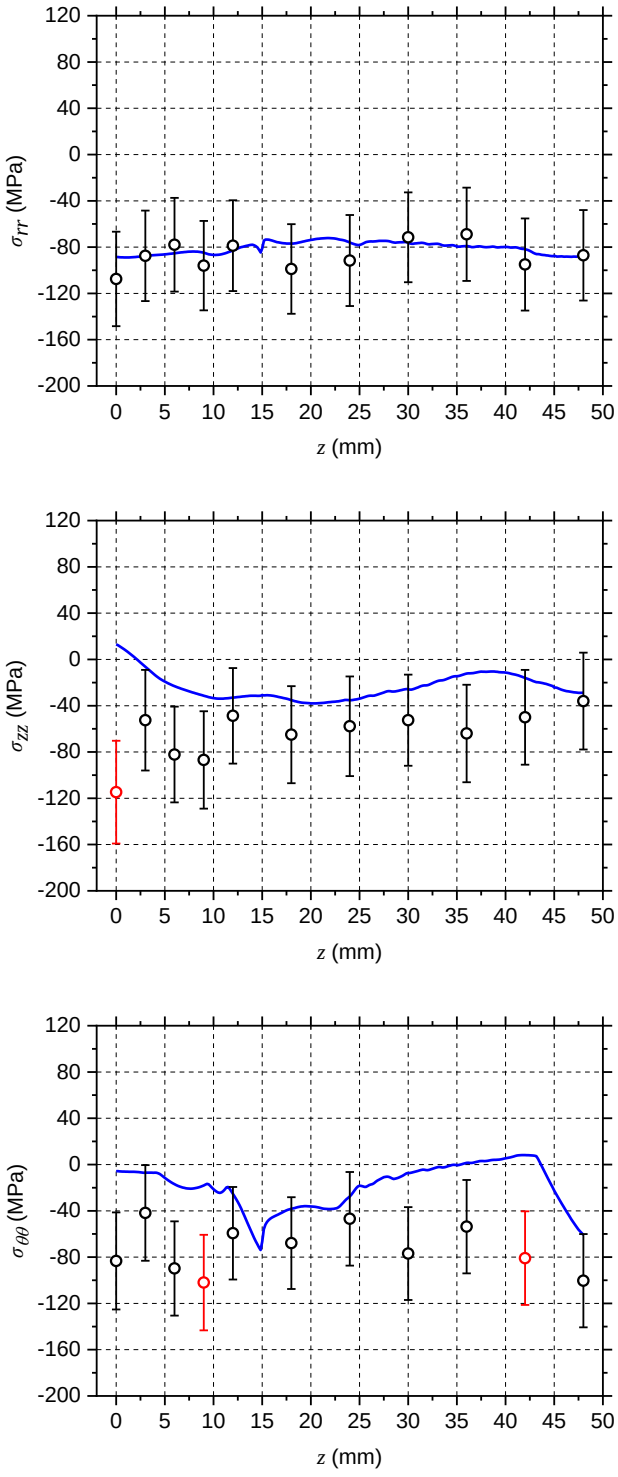


Fig. 17 Measured (circle marks) vs simulated RS (solid line) as a function of the distance from the joint (z) at y = – 8 mm for σ_{rr}, σ_{zz} and $\sigma_{\theta\theta}$. The error bars of data points are also shown. Red symbols: positions in which the measured and simulated RS are not in good agreement

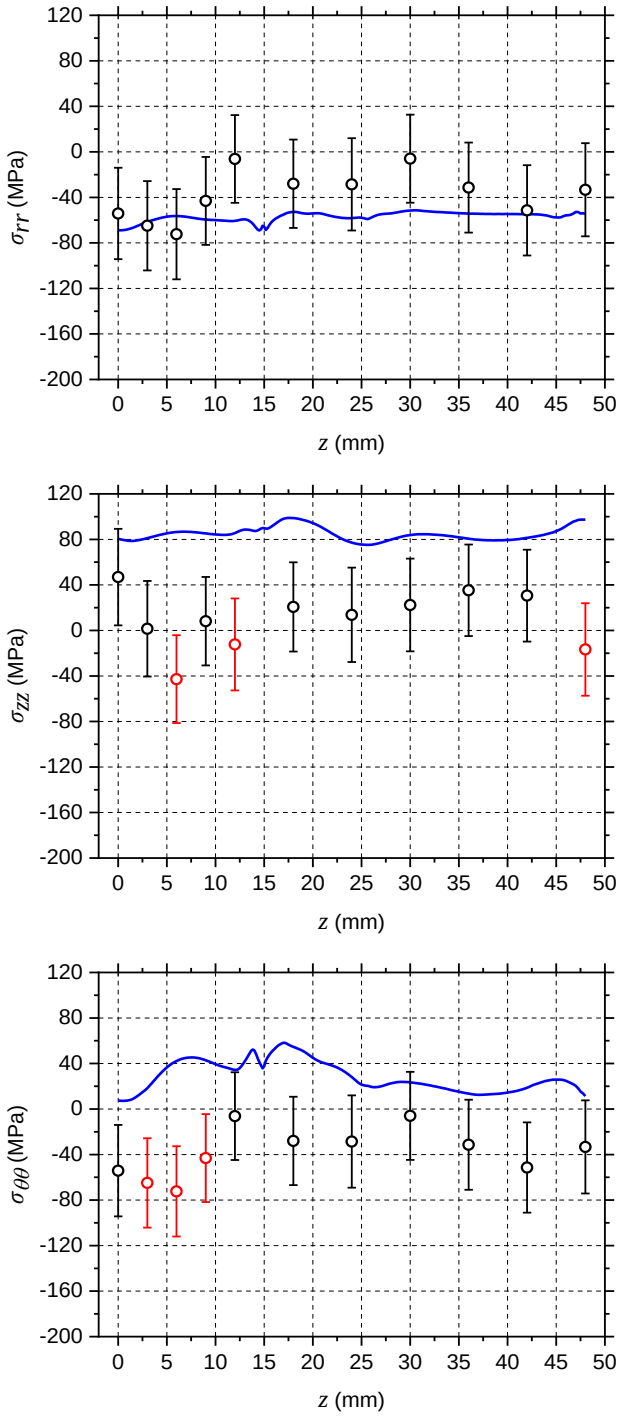


Fig. 18 Measured (circle marks) vs simulated RS (solid line) as a function of the distance from the joint (z) at y = – 11 mm for σ_{rr}, σ_{zz} and $\sigma_{\theta\theta}$. The error bars of data points are also shown. Red symbols: positions in which the measured and simulated RS are not in good agreement

5.2. Residual stress state analysis at the core of the weldment

The core of the weldment was under a compressive stress state in all the measured directions as shown in Fig. 11. Considering that RS generation mechanism is related to the uneven thermal strain field (see Section 3.1), the compressive stress state at the core of the weldment must be related to the temperature field at a particular instant of time of the TLPB thermal cycle. This is indeed the case as shown in Fig. 19 representing the calculated temperature field at the start of the cooling stage. It is worth noting that as the temperatures are higher than 760 ºC (minimum range in the figure) the whole region was partially/fully austenized (the lower and higher critical temperatures on heating are A_{C1} = 725 ºC and A_{C3} = 875 ºC [35] [2]) and transformed into ferrite and pearlite when cooled down to ambient temperature.

It is the large volume in which $\dot{q}$ is delivered at the joint of TLPB weldments during the thermal cycle:

- The simultaneous heating of the whole joint to T_P (1300 ºC)
- The holding time of the whole joint at T_P during t_h (7 min)

which produced this large extension of the partially/fully austenized region and led to low cooling rates with a remarkable t 8/5 of 390 sec. This large value of t 8/5 is a distinctive feature of TLPB compared with AW. Typical values of t 8/5 for AW range from a few seconds for gas tungsten arc welding to less than a minute for submerged arc welding [8].

Consequently, the large volume in which $\dot{q}$ is delivered is the driving force to reduce RS peak magnitudes.

[2] A_{C1} is the temperature which corresponds to the boundary between the ferrite-cementite field and the fields containing austenite and ferrite, while A_{C3} is the temperature which corresponds to the boundary between the ferrite-austenite and austenite fields (during heating of ferritic steels).

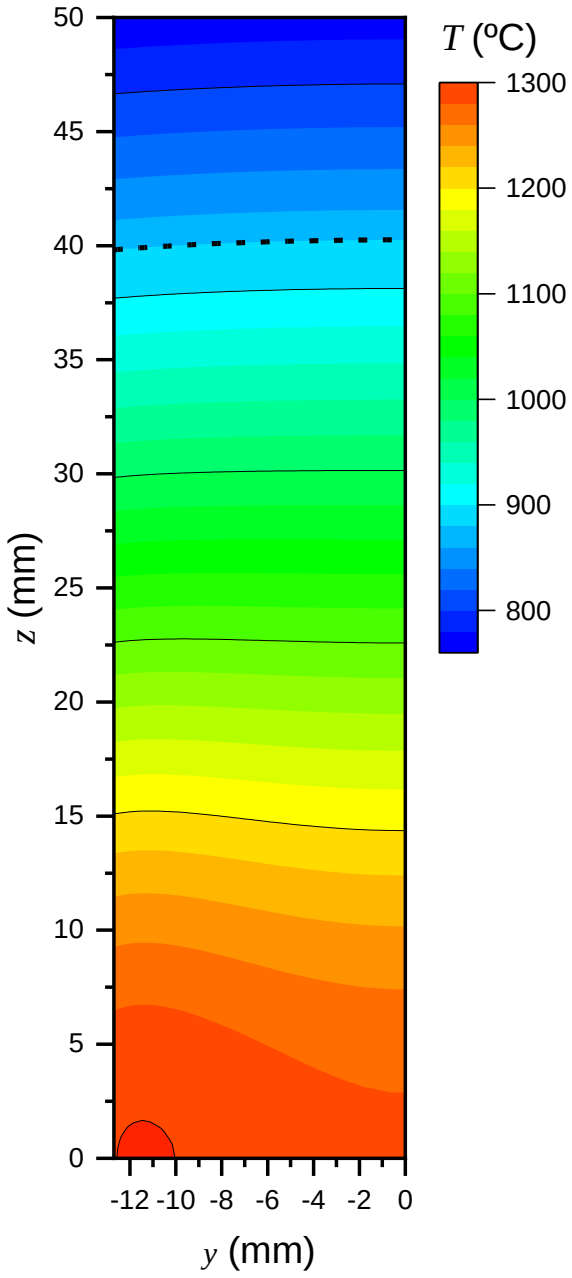


Fig. 19 Calculated temperature field at the start of the cooling stage in the region where RS were scanned. The dashed line indicates A_{C3}, showing that up to 40 mm from the joint full austenization was achieved. Partial austenization is achieved for z > 40 mm

5.3. The heat input and its relationship with the microstructure and the ultimate tensile strength of the weldment

The large volume in which $\dot{q}$ was delivered in TLPB resulted in a wide HAZ with a microstructure composed of coarse-grained ferrite and pearlite (Fig. 9 (b)). This HAZ

microstructure differs from that of the base metal (Fig. 9 (a)). In addition, TLPB low cooling rates lead to mechanically soft high-temperature microconstituents (e.g.: coarse pearlite) [36].

TLPB was successfully applied to low carbon steel structural components using the same filler material as in the present manuscritp – Metglas® SA1 amorphous metallic foil of the Fe-Si-B system with a thickness of 25 μm. The ultimate tensile strength (UTS) of the tested specimens from TLPB weldments carried out in the same manner as in the present work was reported for:

- Hot-rolled seamless steel tubes [37].
- Hot-wrought low carbon steel bars [38].

In both cases, all the tested specimens broke at the HAZ, far from the joint, with a UTS of at least 96% of that of the corresponding base metal.

Therefore, for TLPB of ferritic weldments in the as-welded condition we have an excellent UTS (comparable to the base metal). All together with the low RS peak magnitude (147 MPa) achieved for TLPB these results assess the high performance of this welding process.

6. Conclusions

For the first time the RS field was measured by ND in a TLPB ferritic weldment using Fe-based amorphous metallic foils as filler material. In addition, numerical simulations of the RS field at the weldment were carried out assuming that RS generation mechanism were the result of the uneven thermal strain fields. This included a thermal analysis to determine the temperature field during the thermal cycle of TLPB from which RS were calculated by a mechanical analysis. Finally, the agreement between the measured and simulated RS was analysed.

The main conclusions are:

- The measured RS attained a peak magnitude of 147 MPa in the as-welded condition which are considerably lower compared with AW with values close to σ_y (276 MPa).
- The simulated and measured RS are in good agreement. Therefore, the proposed numerical simulation model can be used to predict RS in TLPB weldments.

- The large volume in which $\dot{q}$ was delivered at the joint of TLPB produced a large extension of the partially/fully austenized region, much lower cooling rates and a large t 8/5.
- The large volume in which $\dot{q}$ is delivered is the driving force to reduce RS peak magnitudes.
- Consequently, TLPB of ferritic weldment offers an UTS which almost attained that of the base metal, while greatly reducing RS in the as-welded condition.

Acknowledgments

This work was partly supported by the Universidad de Buenos Aires [grant number 20020170200266BA].

Neutron experiments were performed at the Institut Max von Laue – Paul Langevin (ILL), Grenoble, France under beam time grant https://dx.doi.org/10.5291/ILL-DATA.DIR-169

The authors acknowledge Metglas® for providing the filler material.

Author contributions

Nicolás Di Luozzo contributed to conceptualization, methodology, software, formal analysis, investigation, writing – original draft, writing – review & editing, visualization, supervision, project administration and funding acquisition. Sandra Cabeza contributed to methodology, software, validation, investigation, data curation, writing – review & editing. Michel Boudard contributed to investigation and writing – review & editing. Marcelo Fontana contributed to resources and writing – review & editing.

Compliance with ethical standards

Conflict of interest The authors declare that they have no conflict of interest.

References

1. Oliveira JP, Barbosa D, Fernandes FMB, Miranda RM (2016) Tungsten inert gas (TIG) welding of Ni-rich NiTi plates: functional behavior. Smart Mater Struct 25:03LT01. https://doi.org/10.1088/0964-1726/25/3/03LT01

2. Oliveira JP, Crispim B, Zeng Z, et al (2019) Microstructure and mechanical properties of gas tungsten arc welded Cu-Al-Mn shape memory alloy rods. J Mater Process Technol 271:93–100. https://doi.org/10.1016/j.jmatprotec.2019.03.020

3. Martin AC, Oliveira JP, Fink C (2020) Elemental Effects on Weld Cracking Susceptibility in AlxCoCrCuyFeNi High-Entropy Alloy. Metall Mater Trans A 51:778–787. https://doi.org/10.1007/s11661-019-05564-8

4. Hemmesi K, Farajian M, Boin M (2017) Numerical studies of welding residual stresses in tubular joints and experimental validations by means of x-ray and neutron diffraction analysis. Mater Des 126:339–350. https://doi.org/10.1016/j.matdes.2017.03.088

5. Balakrishnan J, Vasileiou AN, Francis JA, et al (2018) Residual stress distributions in arc, laser and electron-beam welds in 30 mm thick SA508 steel: A cross-process comparison. Int J Press Vessel Pip 162:59–70. https://doi.org/10.1016/j.ijpvp.2018.03.004

6. Haigh RD, Hutchings MT, James JA, et al (2013) Neutron diffraction residual stress measurements on girth-welded 304 stainless steel pipes with weld metal deposited up to half and full pipe wall thickness. Int J Press Vessel Pip 101:1–11. https://doi.org/10.1016/j.ijpvp.2012.08.003

7. Duvall DS, Owczarski WA, Paulonis DF (1974) TLP Bonding: a New Method for Joining Heat Resistant Alloys. Weld J 53:203–214

8. Kaplan D, Murry G (2008) Thermal, Metallurgical and Mechanical Phenomena in the Heat Affected Zone. In: Metallurgy and Mechanics of Welding. ISTE, London, pp 89–131

9. Fitzpatrick ME, Lodini A (2003) Analysis of Residual Stress by Diffraction using Neutron and Synchrotron Radiation. CRC Press, London

10. Withers PJ (2013) Synchrotron X-ray Diffraction. In: Practical Residual Stress Measurement Methods. John Wiley & Sons, Ltd, Chichester, pp 163–194

11. ASTM A29 / A29M-20 (2020) Standard Specification for General Requirements for Steel Bars, Carbon and Alloy, Hot-Wrought. https://doi.org/10.1520/A0029_A0029M-20

12. ASTM E8 / E8M-21 (2021) Standard Test Methods for Tension Testing of Metallic Materials. https://doi.org/10.1520/E0008_E0008M-21

13. Pirling T, Bruno G, Withers PJ (2006) SALSA—A new instrument for strain imaging in engineering materials and components. Mater Sci Eng A 437:139–144. https://doi.org/10.1016/j.msea.2006.04.083

14. ISO 21432:2019 (2019) Non-destructive testing — Standard test method for determining residual stresses by neutron diffraction

15. Richard D, Ferrand M, Kearley GJ (1996) Analysis and visualisation of neutron-scattering data. J Neutron Res 4:33–39. https://doi.org/10.1080/10238169608200065

16. Behnken H, Hauk V (1986) Berechnung der roentgenographischen Elastizitaetskonstanten (REK) des Vielkristalls aus den Einkristalldaten fuer beliebige Kristallsymmetrie. Zeitschrift für Met 77:620–626

17. Spooner S, Wang X-L (1997) Diffraction Peak Displacement in Residual Stress Samples Due to Partial Burial of the Sampling Volume. J Appl Crystallogr 30:449–455. https://doi.org/10.1107/S0021889897000174

18. Hutchings MT, Withers PJ, Holden TM, Lorentzen T (2005) Introduction to the Characterization of Residual Stress by Neutron Diffraction. CRC Press, Boca Raton

19. Snyder MD, Bathe K-J (1981) A solution procedure for thermo-elastic-plastic and creep problems. Nucl Eng Des 64:49–80. https://doi.org/10.1016/0029-5493(81)90032-7

20. Ueda Y, Murakawa H, Ma N (2012) Chapter 3 - Mechanical Simulation of Welding. In: Ueda Y, Murakawa H, Ma N (eds) Welding Deformation and Residual Stress Prevention. Butterworth-Heinemann, Boston, pp 55–98

21. Rammerstorfer FG, Fischer DF, Mitter W, et al (1981) On thermo-elastic-plastic analysis of heat-treatment processes including creep and phase changes. Comput Struct 13:771–779. https://doi.org/10.1016/0045-7949(81)90040-7

22. Suman S, Biswas P (2020) Comparative study on SAW welding induced distortion and residual stresses of CSEF steel considering solid state phase transformation and preheating. J Manuf Process 51:19–30. https://doi.org/10.1016/j.jmapro.2020.01.012

23. Favennec Y, Labbé V, Bay F (2003) Induction heating processes optimization a general optimal control approach. J Comput Phys 187:68–94. https://doi.org/10.1016/S0021-9991(03)00081-0

24. Labridis D, Dokopoulos P (1989) Calculation of eddy current losses in nonlinear ferromagnetic materials. IEEE Trans. Magn. 25:2665–2669

25. Di Luozzo N, Fontana M, Arcondo B (2012) Modelling of induction heating of carbon steel tubes: Mathematical analysis, numerical simulation and validation. J Alloys Compd 536:S564–S568. https://doi.org/10.1016/j.jallcom.2011.12.084

26. Elmer FEM (2021) Open source multiphysical simulation software. http://www.elmerfem.org/. Accessed 27 Jul 2022

27. BS EN 1993-1-2:2005 (2005) Eurocode 3: Design of steel structures - Part 1-2:

28. Iuchi T, Furukawa T, Wada S (2003) Emissivity modeling of metals during the growth of oxide film and comparison of the model with experimental results. Appl Opt 42:2317. https://doi.org/10.1364/AO.42.002317

29. Churchill SW, Chu HHS (1975) Correlating equations for laminar and turbulent free convection from a horizontal cylinder. Int J Heat Mass Transf 18:1049–1053. https://doi.org/10.1016/0017-9310(75)90222-7

30. Raithby GD, Hollands KGT (1975) A General Method of Obtaining Approximate Solutions to Laminar and Turbulent Free Convection Problems. In: Irvine TF, Hartnett JP (eds). Elsevier, Amsterdam, pp 265–315

31. de Souza Neto E, Perić D, Owen D (2008) Finite Elements in Small-Strain Plasticity Problems. In: Computational Methods for Plasticity. John Wiley & Sons, Ltd, Chichester, pp 191–263

32. Code_Aster (2021) Analysis of Structures and Thermomechanics for Studies & Research. https://code-aster.org/spip.php?rubrique2. Accessed 27 Jul 2022

33. Liu T, Long M, Fan H, et al (2018) Dilatometric determination of four critical temperatures and phase transition fraction for austenite decomposition in hypo-eutectoid steels using peak separation method. J Mater Res 33:967–977. https://doi.org/10.1557/jmr.2017.484

34. Stang AH, Greenspan M, Newman SB (1946) Poisson's ratio of some structural alloys for large strains. J Res Natl Bur Stand (1934) 37:211–221. https://doi.org/10.6028/jres.037.012

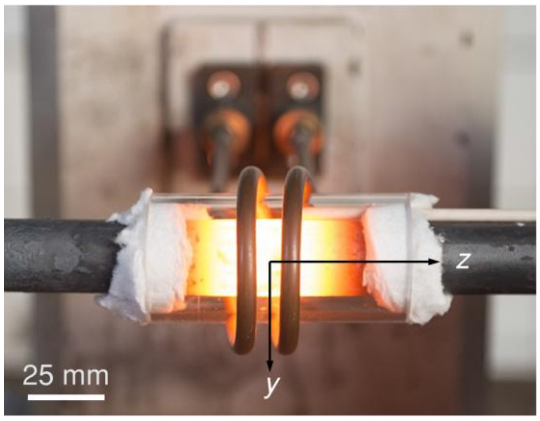
35. Chandler H (1995) Heat Treater's Guide: Practices and Procedures for Irons and Steels, 2nd ed. ASM International, Materials Park, Ohio

36. O’Brien A (2004) Welding Handbook, Volume 2, 9th ed. American Welding Society, Miami

37. Di Luozzo N, Doisneau B, Boudard M, et al (2014) Microstructural and mechanical characterizations of steel tubes joined by transient liquid phase bonding using an amorphous Fe–B–Si interlayer. J Alloys Compd 615:S18–S22. https://doi.org/http://dx.doi.org/10.1016/j.jallcom.2013.11.161

38. Di Luozzo N (2014) Transient liquid phase diffusion welding of metallic parts. https://tel.archives-ouvertes.fr/view/index/identifiant/tel-01297617. Accessed 3 Sep 2022

Transient Liquid Phase Bonding



Measured vs. Simulated Radial Residual Stresses (MPa)

